

Zhen Yao¹ Xin Li² Taotao Jing² Shuai Zhang² Mooi Choo Chuah¹

Abstract

Open-vocabulary semantic segmentation aims to assign labels to every pixel in an image based on text labels. Existing approaches typically utilize Vision-Language Models (VLMs), such as CLIP, for dense prediction. However, VLMs, pre-trained on image-text pairs, are biased toward salient, object-centric regions and exhibit two critical limitations when adapted to segmentation: (i) **Foreground Bias**, which tends to ignore background regions, and (ii) **Limited Spatial Localization**, resulting in blurred object boundaries. To address these limitations, we introduce **DiSa**, a novel saliency-aware foreground-background disentangled framework. By explicitly incorporating saliency cues in our designed Saliency-aware Disentanglement Module (SDM), DiSa separately models foreground and background ensemble features in a divide-and-conquer manner. Additionally, we propose a Hierarchical Refinement Module (HRM) that leverages pixel-wise spatial contexts and enables channel-wise feature refinement through multi-level updates. Extensive experiments on six benchmarks demonstrate that DiSa consistently outperforms state-of-the-art methods.

1. Introduction

Open-vocabulary semantic segmentation aims to label each pixel with an unlimited range of categories that extend beyond a pre-defined closed set, based on text labels. To this end, vision-language models (VLMs), e.g., CLIP (Radford et al., 2021) and ALIGN (Jia et al., 2021), have been widely explored, as they exhibit powerful zero-shot recognition capabilities via large-scale training on image-text pairs.

Despite these advances, VLMs pre-trained on image-text pairs face 2 critical limitations when adapted to dense prediction tasks: (1) **Foreground Bias**: VLMs tend to overem-

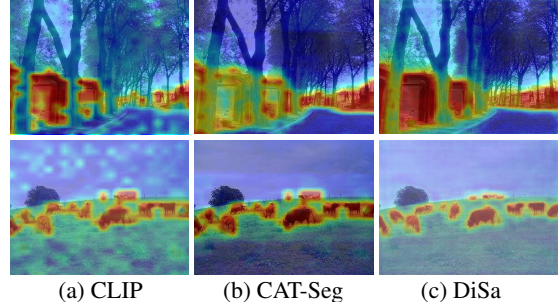


Figure 1. **Visualization of correlation maps.** VLMs face **Foreground Bias** and **Limited Spatial Localization** challenges. Our proposed DiSa effectively alleviates these challenges. Row 1 indicates class “building”, and Row 2 indicates class “animal”.

phasize salient, foreground regions while neglecting background context, leading to misclassification of background regions (Li et al., 2024b). This bias stems from the object-centric nature of pre-training data, where captions predominantly describe salient, foreground instances. This results in a fundamental misalignment between the foreground-centric bias of VLMs and the pixel-level precision of segmentation, which requires holistic scene understanding and accurate recognition of non-salient background regions. As shown in row 1 of Fig. 1, VLMs pay little attention to non-salient, background buildings. (2) **Limited Spatial Localization**: VLMs demonstrate limited capacity of fine-grained spatial reasoning required for segmentation predictions. Due to insufficient dense supervision during pre-training, these models struggle to capture precise object boundaries and reconstruct local structural details (as shown in row 2 of Fig. 1). This poses challenges in distinguishing visually similar or spatially overlapping categories (Lee et al., 2025), particularly for small objects and background regions that require nuanced spatial reasoning for accurate segmentation (Zhou et al., 2022; Zhong et al., 2022).

To address these limitations, we propose foreground-background disentanglement mechanisms to tackle various category roles across different visual contexts. Our design is motivated by the observation that most categories exhibit context-dependent roles, e.g., cars or furniture may appear as either foreground instances or background context depending on scene composition. This contextual distinction highlights the importance of adaptive representa-

¹Department of Computer Science and Engineering, Lehigh University ²Qualcomm AI Research. Correspondence to: Zhen Yao <zhy321@lehigh.edu>.

tion learning that captures both fine-grained localization for foreground instances and the semantic coherence for background regions. While existing approaches explore token-level or class-level disentanglement, they either fail to preserve intra-class relationships or assume rigid taxonomies, leading to sub-optimal performance. To overcome these limitations, we leverage saliency cues for adaptive foreground-background inter-token decomposition for each category. Unlike prior works that merely employ saliency for computational efficiency (Choi et al., 2024; Luo et al., 2024), our method explicitly leverages saliency to address the aforementioned **Foreground Bias** challenge. Specifically, we leverage saliency maps derived from text-image cross-attention to effectively partition per-class visual embeddings into foreground (salient, object-centric) and background (contextual, peripheral) regions based on their corresponding saliency scores. This enables ensemble feature learning via dual branches that capture domain-specific characteristics while preserving semantic coherence.

Building on the saliency-aware disentanglement, we propose a novel framework, DiSa, which explicitly separates foreground and background features. This decomposition enables our model to learn distinct and complementary representations, addressing the inherent imbalance in semantic granularity between foreground and background regions. In addition, we introduce a Hierarchical Refinement Module (HRM) that captures detailed spatial context and refines features via multi-level updates. Specifically, it consists of (1) Pixel-wise Refinement, which enhances spatial localization at the pixel level; (2) Category-wise Refinement, which captures channel-wise coherence for each class; and (3) Semantic-wise Refinement, which extracts semantic consistency within broader foreground/background groupings.

In summary, our contributions in this paper include:

- We propose **DiSa**, a novel Saliency-aware Foreground-background Disentangled framework for OVSS. Our Saliency-aware Disentanglement Module (SDM) is the first to use explicit saliency cues for adaptive intra-class foreground-background decomposition, enabling context-dependent assignment. It facilitates semantic coherence especially for non-salient background regions, mitigating **Foreground Bias**.
- DiSa introduces a Hierarchical Refinement Module (HRM) that captures spatial context through Pixel-, Category-, and Semantic-wise Refinement. By incorporating spatial and channel-level context modeling, HRM alleviates the challenge of **Limited Spatial Localization**, improving fine-grained boundary localization and spatial discrimination capabilities.
- We conduct extensive evaluations across six large-scale open-vocabulary semantic segmentation benchmarks. DiSa consistently outperforms state-of-the-art methods,

achieving significant performance gains that demonstrate its effectiveness and robustness.

2. Related Work

2.1. Open-vocabulary Semantic Segmentation

With the advance of VLMs, researchers have started to explore their powerful visual-text alignment capabilities to provide semantically rich and aligned multimodal representations in this task. SegCLIP (Liu et al., 2024) integrates CLIP with Vision Transformers (ViT) (Dosovitskiy et al., 2020) through a semantic group module that aggregates patches with learnable centers. It additionally introduces two auxiliary losses, one is a reconstruction loss for recovering the masked patches, and another is a superpixel-based KL divergence loss. CAT-Seg (Cho et al., 2024) estimates cost volumes from CLIP image-text similarities, followed by spatial and class aggregation to improve localization accuracy. The cost volumes serve as visual groundings for class-specific predictions. SCAN (Liu et al., 2024) presents a Semantic-assisted Calibration Network to mitigate misalignment between visual contents and text semantics by calibrating the mask proposals and reducing domain bias in CLIP. ESC-Net (Lee et al., 2025) leverages CLIP-derived image-text correlations as pseudo-supervision for SAM, generating accurate predictions through the powerful segmentation capabilities of foundation models.

A parallel line of research investigates saliency for computational efficiency. SBAM (Choi et al., 2024) proposes an adaptive masking mechanism based on saliency-driven importance scores to enhance pre-training efficiency. PnP-OVSS (Luo et al., 2024) introduces a token pruning strategy that constructs class-agnostic saliency maps by aggregating category-specific attention, pruning less discriminative tokens. However, these approaches merely focus on computational optimization rather than leveraging saliency information to address critical limitations in foreground-background disambiguation and spatial localization inherent in VLMs.

2.2. Foreground-background Disentanglement

Recent works identified **Foreground Bias** (Li et al., 2024b) as a fundamental limitation in VLMs, where pre-training on object-centric image-text pairs introduces systematic biases toward salient regions while neglecting holistic scene understanding. To address this issue, researchers explored foreground-background decomposition strategies for ensemble modeling of background regions.

One research direction focuses on decomposing all visual embeddings into foreground and background regions at the token level. Panoptic SegFormer (Li et al., 2022b) presents a query decoupling strategy to adaptively separate visual tokens into thing and stuff queries. OpenSeeD (Zhang et al., 2023) employs language guidance to select foreground queries, which subsequently interact with learnable back-

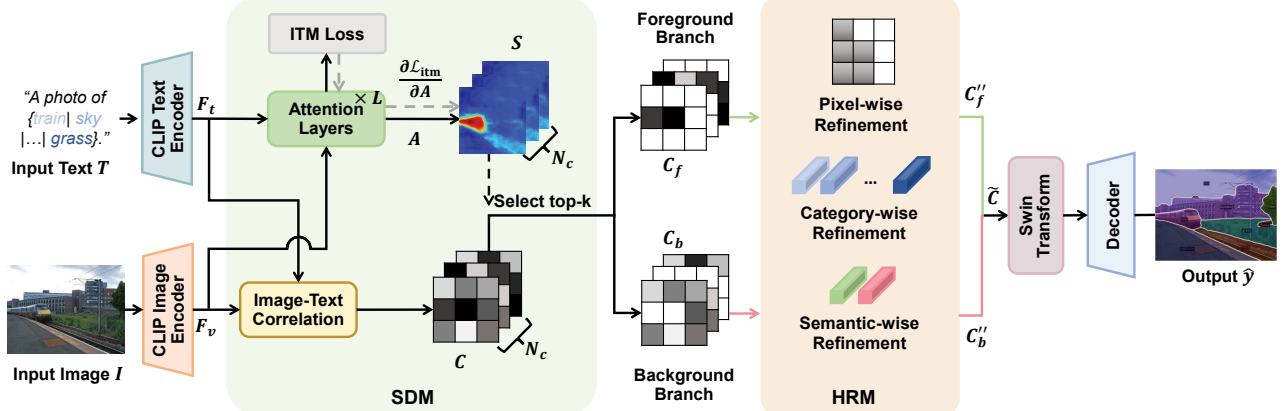


Figure 2. Overview of the DiSa Framework. DiSa consists of a Saliency-aware Disentanglement Module (SDM) and a Hierarchical Refinement Module (HRM), followed by an upsampling decoder.

ground queries through decoupled cross-attention blocks. FOUND (Siméoni et al., 2023) extracts high-confident “seed” tokens to generate coarse background masks through attention maps, enhancing fine-grained object localization. ClearCLIP (Lan et al., 2024) decomposes CLIP vision encoder outputs to attention output and residual connections, learning more robust object recognition. FOCUS (You et al., 2025) leverages two pre-defined prompts to generate foreground/background masks and further calculates the contrastive loss for improved foreground localization.

Alternative approaches perform disentanglement at the class level, separating all classes into foreground and background taxonomies. DenseVLM (Li et al., 2024b) designs a novel VLM that mitigates background imbalance by generating pseudo labels for unlabeled regions using frozen VLM and then applying separate alignment objectives for pre-defined foreground and background categories. Talk2DINO (Barselotti et al., 2024) designs a Background Cleaning Procedure that re-weights class scores based on the self-attention maps, highlighting the foreground regions while suppressing background interference. LBP (Li et al., 2024a) enhances background understanding for open-vocabulary object detection by learning background prompts from other images, effectively incorporating implicit background knowledge and achieving superior performance.

Despite these advances, existing disentanglement approaches suffer from several limitations. Token-level disentanglement fails to preserve intra-class relationships that are crucial for dense predictions. Class-level disentanglement assumes rigid foreground-background taxonomies, ignoring that instances of each class may appear as either foreground or background depending on scene composition. Furthermore, learnable disentanglement modules without any prior knowledge lack explicit guidance and are sub-optimal. In contrast to these approaches, our method leverages explicit saliency supervision to perform adaptive, class-specific foreground-background disentanglement, develop-

ing semantic coherence among ensemble representations while addressing the **Foreground Bias** in VLMs.

3. Methodology

3.1. Motivation

Our approach is motivated by the observation that the challenges of open-vocabulary semantic segmentation lie in the inherent asymmetry between foreground objects (salient, instance-centric elements) and background regions (contextual, peripheral environments), which are often entangled within shared feature spaces. To be more specific, in real-world images, the role of a category can vary based on scene composition (e.g., a train in focus vs. a train in the far background). This aligns with how humans parse visual scenes: we don’t always treat “train” in different scenes with equal attention — it depends on salience, size, occlusion, etc.

While existing methods treat all regions uniformly, we argue that the inherent differences between foreground and background semantics reveal the benefits of a more principled decomposition strategy. This allows both foreground and background features to learn specialized representations and learning objectives, aligning with the “Seek common ground while reserving differences” design ideology (Li et al., 2022b). Even for *stuff* classes, the foreground refers to the most semantically informative or attribute-rich sub-regions. This behavior aligns with our above motivation: even within the same class, different regions may contribute differently to the textual concept. For example, in classes like wall or sky, the textured parts of a wall and the cloud structures in the sky provide relatively stronger visual cues, while others serve as contextual or peripheral background.

To this end, we propose a divide-and-conquer formulation that leverages saliency cues to structurally decompose the segmentation task into two complementary sub-problems: foreground object localization and background region understanding. This separation not only improves robustness

to dynamic scene compositions but also enhances holistic scene understanding by improving disambiguation.

3.2. Architecture Overview

Fig. 2 provides an overview of our proposed framework, DiSa. Our model consists of 4 core components: a CLIP image encoder, a CLIP text encoder, a Saliency-aware Disentanglement Module (SDM) for foreground-background disentanglement, and a Hierarchical Refinement Module (HRM) for integrating multi-level fine-grained details. We follow existing works (Xian et al., 2019; Bucher et al., 2019) for the task design, e.g., the input and output formats. Given an input image I and a set of text labels $T = \{T_i, i = 1, 2, \dots, N_C\}$, where N_C is the number of all C classes, we utilize CLIP as vision-language encoders to extract image $F_v \in \mathbb{R}^{H \times W \times D}$ and text embeddings $F_t \in \mathbb{R}^{N_C \times D}$, where D is the dimension size.

Our proposed pipeline begins by processing image F_v and text embeddings F_t to extract cross-attention maps $A \in \mathbb{R}^{HW \times N_C}$ through SDM. These attention maps are then sharpened by Image-Text Matching (ITM) loss (Li et al., 2021) gradients and the outputs are saliency maps $S_{1:N_C} \in \mathbb{R}^{H \times W \times N_C}$. Meanwhile, DiSa generates correlation maps $C_{1:N_C} \in \mathbb{R}^{H \times W \times N_C \times D}$ between image F_v and text embeddings F_t through cosine similarity and projection MLP layers. All correlation tokens from C are then divided into a Foreground and a Background Branch based on their corresponding saliency scores S . The details of SDM are explained in Section 3.3. Subsequently, we propose a three-stage Hierarchical Refinement Module (HRM) to further enhance the fine-grained localization and semantic precision of disentangled correlation maps C_f and C_b separately via Pixel-wise, Category-wise, and Semantic-wise Refinement. Detailed explanations of HRM are in Section 3.4. Afterwards, the refined features (C''_f and C''_b) from the foreground and background branches are integrated through a weighted feature aggregation block to produce aggregated correlation maps $\tilde{C} \in \mathbb{R}^{H \times W \times N_C \times D}$. Finally, it produces the final mask predictions \hat{y} through an upsampling decoder.

3.3. Saliency-aware Disentanglement Module

We design the SDM to address the inherent **Foreground Bias** in VLMs. It uses GradCAM (Selvaraju et al., 2017) to generate per-class saliency maps from cross-attention. Traditional saliency-based methods merely focus on improving model efficiency through token pruning. However, we incorporate saliency as an additional visual cue to perform complementary feature learning. The saliency is consistent with prior work that reflects semantic contribution but with a slight modification: we obtain saliency maps for each class instead of a single saliency map for all classes. In our method, saliency therefore represents regions of semantic details and informative structures, not merely regions of model confidence. Saliency provides a scalar importance

score for disentanglement. It captures where meaningful evidence appears, while correlation encodes the semantic cues present in that region. The gradient-based saliency generation is essential for robust disentanglement.

Saliency Map Generation. Given image F_v and text embeddings F_t , we employ cross-attention layers where text embeddings serve as the query and image embeddings serve as the key/value. The intermediate attention map A captures image-text correspondences; however, the attentions typically exhibit scattered and spatially diffuse activations due to their overly broad receptive fields, which are inherent in global modeling (Wang et al., 2025). To address this limitation, we selectively suppress less-relevant regions within the attention map A and enhance its spatial precision via gradient-based reweighting. This objective is achieved through an auxiliary Image-Text Matching (ITM) loss \mathcal{L}_{itm} (Li et al., 2021) that provides explicit supervision for localization. Specifically, we append an auxiliary regression head to classify whether each image-text pair is matched. The ITM loss is formulated as:

$$\mathcal{L}_{itm} = \mathbb{E}_{(v,t) \sim D} \mathcal{H}(\hat{y}_{(v,t)}^{itm}, y^{itm}) \quad (1)$$

where \mathcal{H} is the cross-entropy loss, and ground-truth labels y^{itm} are one-hot vectors obtained from segmentation masks. During inference, we use the regressed image-text matching scores $\hat{y}_{(v,t)}^{itm}$ to generate gradients, so no ground truth or class labels are required, thereby avoiding data leakage. Afterwards, we compute the gradient of \mathcal{L}_{itm} and let the attention maps narrowly focus on the most discriminative regions through GradCAM-style re-weighting to produce the saliency map S_n for the n -th class, following PnP-OVSS:

$$S_n = \max \left(0, \frac{\partial \mathcal{L}_{itm}}{\partial A_n} \right) \otimes A_n \quad (2)$$

where \otimes represents element-wise multiplication. Eq. 2 presents the general formulation, while during inference the loss term is replaced by the regressed matching scores and more details are in the appendix. Note that the goal of this auxiliary sharpening loss is to enhance contrast and to back-propagate gradients for saliency generation. The quality of disentanglement is not heavily dependent on the quality and accuracy of it. Instead, we rely on the image-text attention maps A , which provide robust localization cues and are continuously optimized during training through segmentation objectives, thereby stabilizing and enhancing them even if the auxiliary ITM supervision is imperfect.

Foreground/Background Token Selection. Unlike traditional approaches that treat all visual tokens uniformly, we propose a dual-branch mechanism to disentangle all visual tokens into the Foreground and Background Branches by saliency-aware feature decomposition. It enables the model to explicitly distinguish between foreground and

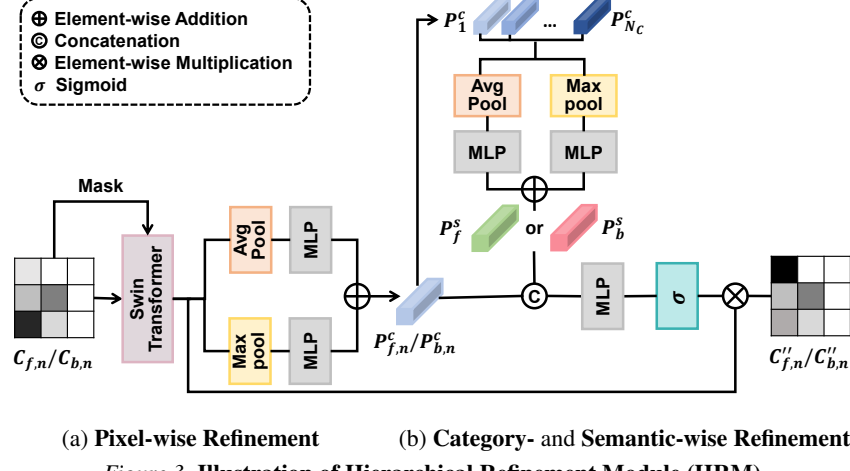


Figure 3. Illustration of Hierarchical Refinement Module (HRM).

background regions, focusing on the distinctive characteristics of both features. This architectural decoupling directly mitigates **Foreground Bias** in VLMs caused by their object-centric focus during pre-training. It enables each branch to develop domain-specific representations.

Specifically, for the n -th class, we select the top- k visual tokens in the correlation maps C_n corresponding to their saliency scores S_n through a binary mask as foreground correlation maps $C_{f,n}$ while the remaining are designated as background correlation maps $C_{b,n}$. These disentangled maps are then processed through two specialized branches: a Foreground Branch that models salient foreground features, and a Background Branch that captures contextual background information.

3.4. Hierarchical Refinement Module

Existing SOTA methods often struggle with effectively capturing the boundary details in complex scenes. To address this challenge, we perform hierarchical refinement to update the correlation maps C across three distinct levels: (1) **Pixel-wise Refinement**, which focuses on achieving precise spatial localization; (2) **Category-wise Refinement**, aimed at enhancing channel-wise coherence for each class; and (3) **Semantic-wise Refinement**, which captures semantic consistency within broader foreground/background groupings. The hierarchical design preserves fine-grained spatial details while capturing cross-channel context, leading to improved segmentation precision in complex visual environments.

Pixel-wise Refinement. As shown in Fig. 3, Pixel-wise Refinement takes foreground correlation maps C_f and background correlation maps C_b as input. The Pixel-wise Refinement block is applied for spatial aggregation based on the Swin Transformer (Liu et al., 2021) block with key modifications. Instead of performing cross-attention across all tokens, we apply masked attention within the block in two branches to focus solely on foreground and background embeddings, respectively. It consists of 2 blocks: the first

block implements attention within a local window, while the second block employs shifted window-based attention to enhance global context integration. The outputs are well-refined correlation maps (C'_f and C'_b) after pixel-wise spatial aggregation, suppressing noise in image-text correlations.

Category-wise Refinement. Subsequent to Pixel-wise Refinement, Category-wise Refinement is applied to consider category-specific cross-covariance across feature channels. Given the pixel-refined correlation maps C'_f and C'_b , we apply 2D global average pooling and max pooling in parallel to extract both the spatial extent of target objects and discriminative clues across channel dimensions. The resulting pooled features are independently processed by 2 MLPs, and their outputs are combined through element-wise addition to generate the category prototype $P^c \in \mathbb{R}^{1 \times N_c \times D}$. Note that the P^c is class-specific, and $P_{f,n}^c$ and $P_{b,n}^c$ represent the category prototype for the n -th class.

Semantic-wise Refinement. While Category-wise Refinement enhances channel-wise coherence, it is class-specific and may overlook broader contextual cues, e.g., surrounding environments or overall scenes among all classes. To improve semantic understanding of the relationship among all salient objects for foreground and all semantic regions in the environments for background, we design the Semantic-wise Refinement. This additional refinement block considers coarse-grained scene context across all classes, leading to more robust and generalized representations.

Similar to Category-wise Refinement, we apply 1D global average pooling and max pooling layers among category prototypes of all classes $\{P_i^c, i = 1, 2, \dots, N_c\}$ to extract semantic prototypes $P^s \in \mathbb{R}^{1 \times 1 \times D}$. Note that P_f^s and P_b^s are class-agnostic and shared among all classes within the Foreground and Background Branches. After extracting both category P^c and semantic prototypes P^s , we update the pixel-refined correlation maps C'_f and C'_b by aggregating these channel-wise cues. Specifically, for the n -th class,

| Model | VLM | Additional Backbone | Training Dataset | Additional Dataset | A-847 | PC-459 | A-150 | PC-59 | PAS-20 | PAS-20 ^b |
|--------------------|---------------|---------------------|------------------|--------------------|-------------|-------------|-------------|-------------|-------------|---------------------|
| LSeg [arXiv21] | CLIP ViT-B/32 | ResNet-101 | PASCAL VOC-15 | ✗ | - | - | - | - | 47.4 | - |
| LSeg+ [ECCV22] | ALIGN | ResNet-101 | COCO-Stuff | ✗ | 2.5 | 5.2 | 13.0 | 36 | - | 59.0 |
| ZegFormer [CVPR22] | CLIP ViT-B/16 | ResNet-101 | COCO-Stuff-156 | ✗ | 4.9 | 9.1 | 16.9 | 42.8 | 86.2 | 62.7 |
| ZegFormer [CVPR22] | CLIP ViT-B/16 | ResNet-101 | COCO-Stuff | ✗ | 5.6 | 10.4 | 18.0 | 45.5 | 89.5 | 65.5 |
| ZSSeg [ECCV22] | CLIP ViT-B/16 | ResNet-101 | COCO-Stuff | ✗ | 7.0 | - | 20.5 | 47.7 | 88.4 | - |
| OpenSeg [ECCV22] | ALIGN | ResNet-101 | COCO Panoptic | ✓ | 4.4 | 7.9 | 17.5 | 40.1 | - | 63.8 |
| OVSeg [CVPR23] | CLIP ViT-B/16 | ResNet-101 | COCO-Stuff | ✓ | 7.1 | 11.0 | 24.8 | 53.3 | 92.6 | - |
| ZegCLIP [CVPR23] | CLIP ViT-B/16 | - | COCO-Stuff-156 | ✗ | - | - | - | 41.2 | 93.6 | - |
| SAN [CVPR23] | CLIP ViT-B/16 | - | COCO-Stuff | ✗ | 10.1 | 12.6 | 27.5 | 53.8 | 94.0 | - |
| EBSeg [CVPR24] | CLIP ViT-B/16 | - | COCO-Stuff | ✗ | 11.1 | 17.3 | 30.0 | 56.7 | 94.6 | - |
| SED [CVPR24] | ConvNeXt-B | - | COCO-Stuff | ✗ | 11.4 | 18.6 | 31.6 | 57.3 | 94.4 | - |
| CAT-Seg [CVPR24] | CLIP ViT-B/16 | - | COCO-Stuff | ✗ | <u>12.0</u> | 19.0 | 31.8 | 57.5 | 94.6 | <u>77.3</u> |
| DPSeg [CVPR25] | CLIP ViT-B/16 | - | COCO-Stuff | ✗ | <u>12.0</u> | <u>19.5</u> | <u>32.9</u> | <u>58.1</u> | <u>96.0</u> | - |
| DiSa | CLIP ViT-B/16 | - | COCO-Stuff | ✗ | 12.6 | 20.3 | 33.7 | 59.3 | 97.0 | 79.9 |
| | | | | | (+0.6) | (+0.8) | (+0.8) | (+1.2) | (+1.0) | (+2.6) |
| LSeg [arXiv21] | CLIP ViT-B/32 | ViT-L/16 | PASCAL VOC-15 | ✗ | - | - | - | - | 52.3 | - |
| OpenSeg [ECCV22] | ALIGN | Eff-B7 | COCO Panoptic | ✓ | 8.1 | 11.5 | 26.4 | 44.8 | - | 70.2 |
| OVSeg [CVPR23] | CLIP ViT-L/14 | Swin-B | COCO-Stuff | ✓ | 9.0 | 12.4 | 29.6 | 55.7 | 94.5 | - |
| SAN [CVPR23] | CLIP ViT-L/14 | - | COCO-Stuff | ✗ | 12.4 | 15.7 | 32.1 | 57.7 | 94.6 | - |
| ODISE [CVPR23] | CLIP ViT-L/14 | Stable Diffusion | COCO-Stuff | ✗ | 11.1 | 14.5 | 29.9 | 57.3 | - | - |
| SCAN [CVPR24] | CLIP ViT-L/14 | - | COCO-Stuff | ✗ | 14.0 | 16.7 | 33.5 | 59.3 | 97.2 | - |
| EBSeg [CVPR24] | CLIP ViT-L/14 | - | COCO-Stuff | ✗ | 13.7 | 21.0 | 32.8 | 60.2 | 96.4 | - |
| SED [CVPR24] | ConvNeXt-L | - | COCO-Stuff | ✗ | 13.9 | 22.6 | 35.2 | 60.6 | 96.1 | - |
| CAT-Seg [CVPR24] | CLIP ViT-L/14 | - | COCO-Stuff | ✗ | <u>16.0</u> | <u>23.8</u> | <u>37.9</u> | <u>63.3</u> | 97.0 | <u>82.5</u> |
| DPSeg [CVPR25] | CLIP ViT-L/14 | - | COCO-Stuff | ✗ | 14.9 | 23.5 | 36.4 | 62.0 | 97.4 | - |
| DiSa | CLIP ViT-L/14 | - | COCO-Stuff | ✗ | 16.3 | 24.9 | 38.9 | 64.7 | 98.7 | 84.7 |
| | | | | | (+0.3) | (+1.1) | (+1.0) | (+1.4) | (+1.3) | (+2.2) |

Table 1. Quantitative results on 6 benchmarks. The best-performing results are presented in **bold**, while the second-best results are underlined. Improvements over the second-best are in **bold**.

we fuse both P_n^c and P_n^s by concatenation. Note that the semantic prototype used is selected based on the branch: P_f^s for the Foreground Branch and P_b^s for the Background Branch. This fused output is then element-wise multiplied by pixel-refined correlation embeddings C' , followed by a sigmoid activation:

$$C''_{f,i} = C'_{f,i} \otimes \sigma(\text{MLP}(\text{Concat}(P_{f,i}^c, P_{f,i}^s))) \quad (3)$$

$$C''_{b,i} = C'_{b,i} \otimes \sigma(\text{MLP}(\text{Concat}(P_{b,i}^c, P_{b,i}^s))) \quad (4)$$

where $i = 1, 2, \dots, N_C$, Concat is concatenation, $\sigma(\cdot)$ is sigmoid, and \otimes refers to element-wise multiplication.

By hierarchically refining correlation maps across pixel-, category-, and semantic-levels, HRM makes the saliency-aware correlation representations more informative and enhances the accuracy, leading to fine-grained spatial precision in downstream segmentation tasks.

3.5. Foreground and Background Aggregation

To uniformly model all pixels after capturing foreground- and background-specific features, we use learnable weights by gating mechanism to aggregate disentangled refined correlation maps ($C''_{f,n}$ and $C''_{b,n}$) for the n -th class with previous binary mask (reorganization based on mask indices). We further employ a Swin Transformer block to mitigate potential misalignment between dual branches, and the aggregated correlation maps are denoted as \tilde{C} . Finally, \tilde{C} serves as visual guidance and are fed into an upsampling decoder, along with image embeddings F_v from the CLIP image encoder, to generate the final mask predictions \hat{y} .

4. Experiments

4.1. Datasets

Our experiments are trained on COCO-Stuff (Caesar et al., 2018) and evaluated on 6 large-scale semantic segmentation datasets. **ADE20K** (Zhou et al., 2019) is a large-scale benchmark for semantic segmentation with 2000 validation images, supporting two evaluation protocols: ADE-150 with 150 categories, and ADE-847 with extended 847 classes. **PASCAL-VOC** (Everingham et al., 2010) is a widely used dataset containing 1,500 validation images with 20 foreground categories, referred as PAS-20. Another evaluation protocol PAS-20^b (Ghiasi et al., 2022) with one extra class for background is also included. **PASCAL-Context** (Motaghi et al., 2014) extends PASCAL VOC, supporting 2 evaluation protocols: PC-59 with 59 labeled classes and PC-459 with 459 categories.

4.2. Implementation Details

We implement our work using PyTorch (Paszke, 2019) and Detectron2 (Wu et al., 2019). The loss function is a weighted sum of cross-entropy loss (1) and the ITM loss (0.2). We set $D = 128$, and training resolution to 384×384 . The k value for selecting foreground tokens is 96. The decoder consists of 2 transposed convolution layers that take \tilde{C} and F_v as inputs. Following CAT-Seg (Cho et al., 2024), we fine-tune query/key in attention of CLIP image and text encoders. We train the model using the AdamW optimizer (Loshchilov & Hutter, 2017) with batch size 2. The learning rate is 2e-4 for our designed modules and 2e-6 for CLIP encoders. We use 2 NVIDIA RTX A5000 GPUs for training. All models are trained for 80,000 iterations.



Figure 4. Qualitative results compared to CAT-Seg. DiSa produces more accurate predictions of small objects and visually-similar regions compared to existing SOTA methods. More qualitative results are in the appendix.

4.3. Quantitative Results

Table 1 demonstrates quantitative results on standard OVSS datasets (Zhou et al., 2019; Everingham et al., 2010; Mottaghi et al., 2014). We compare existing works, LSeg (Li et al., 2022a), LSeg+ (Ghiasi et al., 2022), ZegFormer (Ding et al., 2022), ZSseg (Xu et al., 2022), OpenSeg (Ghiasi et al., 2022), OVSeg (Liang et al., 2023), ZegCLIP (Zhou et al., 2023), SAN (Xu et al., 2023b), ODISE (Xu et al., 2023a), SCAN (Liu et al., 2024), EBSeg (Shan et al., 2024), SED (Xie et al., 2024), CAT-Seg (Cho et al., 2024), and DPSeg (Zhao et al., 2025) with similar-scale VLMs. Note that we adopt the DPSeg (Zhao et al., 2025) inference I model for fair comparison. Unlike some prior works, our model does not leverage any additional datasets or backbones.

Our method, DiSa, achieves consistent and significant gains across all benchmarks, in both base-VLM and large-VLM settings. As shown in Table 1, in the base-VLM configuration, DiSa outperforms prior SOTA approaches with the improvements of +0.6%, +0.8%, +0.8%, +1.2%, +1.0%, and +2.6% mIoU (with an average performance gain of +1.2% mIoU), on A-847, PC-459, A-150, PC-59, PAS-20, and PAS-20^b, respectively. For the large-VLM configuration, DiSa outperforms the best prior SOTA by +0.3%, +1.1%, +1.0%, +1.4%, +1.3%, and +2.2% mIoU with an average gain of 1.2% mIoU among all datasets. Note that DiSa has the most significant relative performance gains on PAS-20^b, demonstrating that it mitigates **Foreground Bias**. These gains are not only statistically meaningful but also practi-

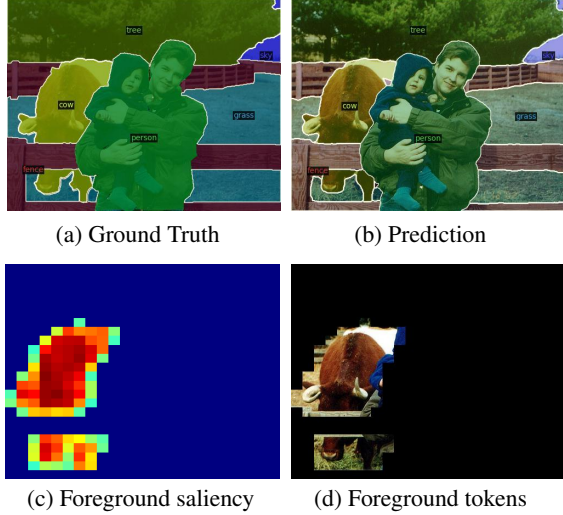


Figure 5. Qualitative comparison of saliency and predictions.

cally significant given the performance saturation observed in this task.

We attribute the leading performance of DiSa to two factors: (1) Our Saliency-aware Disentanglement enhances context-aware features while preserving semantic coherence. It mitigates **Foreground Bias**, as demonstrated by significant improvements on PAS-20^b, which includes background classes. (2) Hierarchical Refinement Module yields accurate and robust boundaries via multi-level refinement, contributing to consistent performance gains across all datasets.

| Model | # Params. (M) | GFLOPs | Inference time (s) |
|-----------|---------------|----------|--------------------|
| ZegFormer | 531.2 | 19,425.6 | 3.10 |
| ZSSeg | 530.8 | 22,302.1 | 3.11 |
| OVSeg | 532.6 | 19,345.6 | 2.98 |
| CAT-Seg | 433.7 | 2,121.1 | 0.78 |
| ESC-Net | 451.3 | 2,203.5 | 0.76 |
| Ours | 456.2 | 2,287.3 | 0.69 |

Table 2. Model complexity comparison. We use CLIP ViT-B/16 for VLM and one single A6000 GPU for fair comparison.

| Decomposition | A-847 | PC-459 | A-150 | PC-59 | PAS-20 | PAS-20 ^b |
|------------------------|-------|--------|-------|-------|--------|---------------------|
| (I) No disentanglement | 11.4 | 18.8 | 30.9 | 56.3 | 94.5 | 76.1 |
| (II) Token-level | 12.1 | 19.9 | 32.6 | 58.2 | 94.5 | 78.9 |
| (III) Class-level | 11.5 | 19.5 | 31.1 | 58.2 | 95.1 | 78.5 |
| (IV) DiSa w/o HRM | 11.7 | 18.7 | 31.2 | 57.7 | 95.3 | 78.5 |
| (V) (IV) + Pixel | 12.4 | 19.5 | 32.3 | 58.8 | 95.9 | 78.9 |
| (VI) (IV) + Category | 11.8 | 19.1 | 32.0 | 57.9 | 95.4 | 78.3 |
| (VII) (V) + Category | 12.5 | 19.8 | 33.1 | 59.0 | 96.6 | 79.1 |
| (VIII) Ours | 12.6 | 20.3 | 33.7 | 59.3 | 97.0 | 79.9 |

Table 3. Ablation study for various design choices. CLIP ViT-B/16 is used as VLM for ablation.

4.4. Qualitative Results

We evaluate qualitative results of our method with CAT-Seg (Cho et al., 2024) using default settings in Fig. 4. We present diverse scenarios, including crowded background (columns 1&5) and visually similar classes (rows 2-4). CAT-Seg struggles to handle complex foreground-background relations and locate accurate boundaries. For example, in column 1, the background is misclassified as “train”. Similarly, in columns 2&4, CAT-Seg produces ambiguous boundaries between visually similar categories (e.g., “snow” and “grass”), reflecting its limited spatial localization. In contrast, DiSa preserves object integrity in crowded scenes, demonstrating superior robustness in challenging scenarios.

We present visualizations of foreground saliency and image tokens of a specific class “cow” in Fig. 5. We observe that foreground and background tokens of the partially occluded cow are identified and not suppressed by other categories. It is consistent with our design, yielding sharper boundaries.

4.5. Model Efficiency Analysis

We further conduct the model efficiency analysis (parameter size and GFLOPS) on all 6 datasets in Table 2. We report the mean run-time on five datasets, following (Cho et al., 2024). Notably, ZegFormer (Ding et al., 2022), ZSSeg (Xu et al., 2022), and OVSeg (Liang et al., 2023) rely on large-scale backbones and complex vision-language fusion modules, with more than 530M parameters and 19k GFLOPs. In contrast, our model significantly reduces inference cost to 2k GFLOPs while maintaining a competitive parameter count of 456M. Although slightly larger than CAT-Seg (Cho et al., 2024) and ESC-Net (Lee et al., 2025), our framework achieves comparable efficiency and remains lightweight compared to other CLIP-based methods. Our gradient-based computation is lightweight because the gradient is only back-propagated to attention maps, not through the entire network. This is a very short computational path with

minimal overhead of the saliency process.

4.6. Ablation Study

Design choices for disentanglement. To validate the impact of our saliency-aware disentanglement, we compare our (I) baseline (DiSa without FG/BG disentanglement which only contains single branch for all tokens) with 2 other designs in Table 3: (II) token-level, following PraNet (Hu et al., 2025) to decouple foreground/background features via FB/BG supervision, (III) class-level, leveraging LLMs (Achiam et al., 2023) for a pre-defined taxonomy and separating all classes into 2 branches. As shown in the table, token-level disentanglement (II) achieves marginal improvements over the baseline (with an average gain of 0.66%). Class-level disentanglement (III) slightly improves on some benchmarks, likely due to its rigidity in adapting to varying scene contexts. In contrast, our proposed saliency-aware disentanglement (VIII) consistently outperforms other decompositions by 1.1% (token-level) and 1.5% (class-level) on average. Notably, it yields a substantial improvement (2.6%) on PAS-20^b, effectively alleviating **Foreground Bias**.

Component analysis for HRM. To validate the effectiveness of HRM, we further evaluate the performance gain of four variants (IV-VII) by gradually adding the components in Table 3. Specifically, they are: (IV) baseline (DiSa without HRM), (V) adding Pixel-wise Refinement to (IV), (VI) adding Category-wise Refinement to (IV), (VII) adding Category-wise Refinement to (V), and (VIII) employing all designed components. Introducing Pixel-wise Refinement (V) improves the average mIoU by 0.78%. Adding Category-wise Refinement (VII) further boosts performance by capturing channel-wise category semantics, with an average gain of 1% over the baseline. Finally, incorporating Semantic-wise Refinement (VIII) yields the highest overall performance (1.62% on average). It demonstrates that HRM and multi-level refinement are essential for mitigating **Limited Spatial Localization** and semantic coherence.

5. Conclusion

In this paper, we propose DiSa, a novel Saliency-aware Foreground-background Disentangled framework for open-vocabulary semantic segmentation. To address the **Foreground Bias** and **Limited Spatial Localization** limitations inherent in VLMs, we propose a Saliency-aware Disentanglement Module (SDM), which performs adaptive foreground-background decomposition based on saliency cues, enabling context-dependent ensemble feature learning. Additionally, by integrating a Hierarchical Refinement Module (HRM), DiSa yields fine-grained spatial localization through Pixel-, Category-, and Semantic-wise Refinement. Extensive experimental results on six large-scale datasets demonstrate the effectiveness of our model. Our observations and novel design shift the paradigm and suggest a promising direction for future research.

Impact Statement

Our work aims to advance open-vocabulary semantic segmentation by explicitly disentangling foreground and background semantics when leveraging vision-language priors. Concretely, we separate class-related evidence into foreground-focused cues and context/background cues, and then reason over each stream (and their interaction) to better capture both object identity and scene context. This foreground/background disentanglement helps alleviate the common bias of pretrained VLMs toward salient object regions while under-representing contextual semantics, improving generalization to novel concepts and reducing dependence on dense pixel-level annotation.

References

Achiam, J., Adler, S., Agarwal, S., Ahmad, L., Akkaya, I., Aleman, F. L., Almeida, D., Altenschmidt, J., Altman, S., Anadkat, S., et al. Gpt-4 technical report. *arXiv preprint arXiv:2303.08774*, 2023.

Barsellotti, L., Bianchi, L., Messina, N., Carrara, F., Cornia, M., Baraldi, L., Falchi, F., and Cucchiara, R. Talking to dino: Bridging self-supervised vision backbones with language for open-vocabulary segmentation. *arXiv preprint arXiv:2411.19331*, 2024.

Bucher, M., Vu, T.-H., Cord, M., and Pérez, P. Zero-shot semantic segmentation. *Advances in Neural Information Processing Systems*, 32, 2019.

Caesar, H., Uijlings, J., and Ferrari, V. Coco-stuff: Thing and stuff classes in context. In *Proceedings of the IEEE conference on computer vision and pattern recognition*, pp. 1209–1218, 2018.

Cheng, B., Misra, I., Schwing, A. G., Kirillov, A., and Girdhar, R. Masked-attention mask transformer for universal image segmentation. In *Proceedings of the IEEE/CVF conference on computer vision and pattern recognition*, pp. 1290–1299, 2022.

Cho, S., Shin, H., Hong, S., Arnab, A., Seo, P. H., and Kim, S. Cat-seg: Cost aggregation for open-vocabulary semantic segmentation. In *Proceedings of the IEEE/CVF Conference on Computer Vision and Pattern Recognition*, pp. 4113–4123, 2024.

Choi, H., Park, H., Yi, K. M., Cha, S., and Min, D. Salience-based adaptive masking: revisiting token dynamics for enhanced pre-training. In *European Conference on Computer Vision*, pp. 343–359. Springer, 2024.

Ding, J., Xue, N., Xia, G.-S., and Dai, D. Decoupling zero-shot semantic segmentation. In *Proceedings of the IEEE/CVF conference on computer vision and pattern recognition*, pp. 11583–11592, 2022.

Dosovitskiy, A., Beyer, L., Kolesnikov, A., Weissenborn, D., Zhai, X., Unterthiner, T., Dehghani, M., Minderer, M., Heigold, G., Gelly, S., et al. An image is worth 16x16 words: Transformers for image recognition at scale. *arXiv preprint arXiv:2010.11929*, 2020.

Everingham, M., Van Gool, L., Williams, C. K., Winn, J., and Zisserman, A. The pascal visual object classes (voc) challenge. *International journal of computer vision*, 88: 303–338, 2010.

Ghiasi, G., Gu, X., Cui, Y., and Lin, T.-Y. Scaling open-vocabulary image segmentation with image-level labels. In *European conference on computer vision*, pp. 540–557. Springer, 2022.

Gotmare, A., Keskar, N. S., Xiong, C., and Socher, R. A closer look at deep learning heuristics: Learning rate restarts, warmup and distillation. *arXiv preprint arXiv:1810.13243*, 2018.

Hu, B.-C., Ji, G.-P., Shao, D., and Fan, D.-P. Pranet-v2: Dual-supervised reverse attention for medical image segmentation. *arXiv preprint arXiv:2504.10986*, 2025.

Jia, C., Yang, Y., Xia, Y., Chen, Y.-T., Parekh, Z., Pham, H., Le, Q., Sung, Y.-H., Li, Z., and Duerig, T. Scaling up visual and vision-language representation learning with noisy text supervision. In *International conference on machine learning*, pp. 4904–4916. PMLR, 2021.

Lan, M., Chen, C., Ke, Y., Wang, X., Feng, L., and Zhang, W. Clearclip: Decomposing clip representations for dense vision-language inference. In *European Conference on Computer Vision*, pp. 143–160. Springer, 2024.

Lee, M., Cho, S., Lee, J., Yang, S., Choi, H., Kim, I.-J., and Lee, S. Effective sam combination for open-vocabulary semantic segmentation. In *Proceedings of the Computer Vision and Pattern Recognition Conference*, pp. 26081–26090, 2025.

Li, B., Weinberger, K. Q., Belongie, S., Koltun, V., and Ranftl, R. Language-driven semantic segmentation. *arXiv preprint arXiv:2201.03546*, 2022a.

Li, J., Selvaraju, R., Gotmare, A., Joty, S., Xiong, C., and Hoi, S. C. H. Align before fuse: Vision and language representation learning with momentum distillation. *Advances in neural information processing systems*, 34: 9694–9705, 2021.

Li, J., Zhang, J., Li, J., Li, G., Liu, S., Lin, L., and Li, G. Learning background prompts to discover implicit knowledge for open vocabulary object detection. In *Proceedings of the IEEE/CVF Conference on Computer Vision and Pattern Recognition*, pp. 16678–16687, 2024a.

Li, Y., Li, Y., Zeng, Q., Wang, W., Hou, Q., and Cheng, M.-M. Densevlm: A retrieval and decoupled alignment framework for open-vocabulary dense prediction. *arXiv preprint arXiv:2412.06244*, 2024b.

Li, Z., Wang, W., Xie, E., Yu, Z., Anandkumar, A., Alvarez, J. M., Luo, P., and Lu, T. Panoptic segformer: Delving deeper into panoptic segmentation with transformers. In *Proceedings of the IEEE/CVF conference on computer vision and pattern recognition*, pp. 1280–1289, 2022b.

Liang, F., Wu, B., Dai, X., Li, K., Zhao, Y., Zhang, H., Zhang, P., Vajda, P., and Marculescu, D. Open-vocabulary semantic segmentation with mask-adapted clip. In *Proceedings of the IEEE/CVF conference on computer vision and pattern recognition*, pp. 7061–7070, 2023.

Liu, Y., Bai, S., Li, G., Wang, Y., and Tang, Y. Open-vocabulary segmentation with semantic-assisted calibration. In *Proceedings of the IEEE/CVF Conference on Computer Vision and Pattern Recognition*, pp. 3491–3500, 2024.

Liu, Z., Lin, Y., Cao, Y., Hu, H., Wei, Y., Zhang, Z., Lin, S., and Guo, B. Swin transformer: Hierarchical vision transformer using shifted windows. In *Proceedings of the IEEE/CVF international conference on computer vision*, pp. 10012–10022, 2021.

Loshchilov, I. and Hutter, F. Decoupled weight decay regularization. *arXiv preprint arXiv:1711.05101*, 2017.

Luo, J., Khandelwal, S., Sigal, L., and Li, B. Emergent open-vocabulary semantic segmentation from off-the-shelf vision-language models. In *Proceedings of the IEEE/CVF Conference on Computer Vision and Pattern Recognition*, pp. 4029–4040, 2024.

Mottaghi, R., Chen, X., Liu, X., Cho, N.-G., Lee, S.-W., Fidler, S., Urtasun, R., and Yuille, A. The role of context for object detection and semantic segmentation in the wild. In *Proceedings of the IEEE conference on computer vision and pattern recognition*, pp. 891–898, 2014.

Paszke, A. Pytorch: An imperative style, high-performance deep learning library. *arXiv preprint arXiv:1912.01703*, 2019.

Radford, A., Kim, J. W., Hallacy, C., Ramesh, A., Goh, G., Agarwal, S., Sastry, G., Askell, A., Mishkin, P., Clark, J., et al. Learning transferable visual models from natural language supervision. In *International conference on machine learning*, pp. 8748–8763. PMLR, 2021.

Selvaraju, R. R., Cogswell, M., Das, A., Vedantam, R., Parikh, D., and Batra, D. Grad-cam: Visual explanations from deep networks via gradient-based localization. In *Proceedings of the IEEE international conference on computer vision*, pp. 618–626, 2017.

Shan, X., Wu, D., Zhu, G., Shao, Y., Sang, N., and Gao, C. Open-vocabulary semantic segmentation with image embedding balancing. In *Proceedings of the IEEE/CVF Conference on Computer Vision and Pattern Recognition*, pp. 28412–28421, 2024.

Siméoni, O., Sekkat, C., Puy, G., Vobecký, A., Zablocki, É., and Pérez, P. Unsupervised object localization: Observing the background to discover objects. In *Proceedings of the IEEE/CVF conference on computer vision and pattern recognition*, pp. 3176–3186, 2023.

Wang, Y., Ni, J., Liu, Y., Yuan, C., and Tang, Y. Iterprime: Zero-shot referring image segmentation with iterative grad-cam refinement and primary word emphasis. In *Proceedings of the AAAI Conference on Artificial Intelligence*, volume 39, pp. 8159–8168, 2025.

Wu, Y., Kirillov, A., Massa, F., Lo, W.-Y., and Girshick, R. Detectron2. <https://github.com/facebookresearch/detectron2>, 2019.

Xian, Y., Choudhury, S., He, Y., Schiele, B., and Akata, Z. Semantic projection network for zero-and few-label semantic segmentation. In *Proceedings of the IEEE/CVF Conference on Computer Vision and Pattern Recognition*, pp. 8256–8265, 2019.

Xie, B., Cao, J., Xie, J., Khan, F. S., and Pang, Y. Sed: A simple encoder-decoder for open-vocabulary semantic segmentation. In *Proceedings of the IEEE/CVF conference on computer vision and pattern recognition*, pp. 3426–3436, 2024.

Xu, J., Liu, S., Vahdat, A., Byeon, W., Wang, X., and De Mello, S. Open-vocabulary panoptic segmentation with text-to-image diffusion models. In *Proceedings of the IEEE/CVF conference on computer vision and pattern recognition*, pp. 2955–2966, 2023a.

Xu, M., Zhang, Z., Wei, F., Lin, Y., Cao, Y., Hu, H., and Bai, X. A simple baseline for open-vocabulary semantic segmentation with pre-trained vision-language model. In *European Conference on Computer Vision*, pp. 736–753. Springer, 2022.

Xu, M., Zhang, Z., Wei, F., Hu, H., and Bai, X. Side adapter network for open-vocabulary semantic segmentation. In *Proceedings of the IEEE/CVF conference on computer vision and pattern recognition*, pp. 2945–2954, 2023b.

You, Z., Kong, L., Meng, L., and Wu, Z. Focus: Towards universal foreground segmentation. In *Proceedings of the AAAI Conference on Artificial Intelligence*, volume 39, pp. 9580–9588, 2025.

Zhang, H., Li, F., Zou, X., Liu, S., Li, C., Yang, J., and Zhang, L. A simple framework for open-vocabulary segmentation and detection. In *Proceedings of the IEEE/CVF International Conference on Computer Vision*, pp. 1020–1031, 2023.

Zhao, Z., Li, X., Shi, L., Imanpour, N., and Wang, S. Dpseg: Dual-prompt cost volume learning for open-vocabulary semantic segmentation. In *Proceedings of the Computer Vision and Pattern Recognition Conference*, pp. 25346–25356, 2025.

Zhong, Y., Yang, J., Zhang, P., Li, C., Codella, N., Li, L. H., Zhou, L., Dai, X., Yuan, L., Li, Y., et al. Regionclip: Region-based language-image pretraining. In *Proceedings of the IEEE/CVF conference on computer vision and pattern recognition*, pp. 16793–16803, 2022.

Zhou, B., Zhao, H., Puig, X., Xiao, T., Fidler, S., Barriuso, A., and Torralba, A. Semantic understanding of scenes through the ade20k dataset. *International Journal of Computer Vision*, 127:302–321, 2019.

Zhou, C., Loy, C. C., and Dai, B. Extract free dense labels from clip. In *European Conference on Computer Vision*, pp. 696–712. Springer, 2022.

Zhou, Z., Lei, Y., Zhang, B., Liu, L., and Liu, Y. Zegclip: Towards adapting clip for zero-shot semantic segmentation. In *Proceedings of the IEEE/CVF conference on computer vision and pattern recognition*, pp. 11175–11185, 2023.

Appendix Overview

In this Appendix, we provide additional details of the paper, including other inference-time saliency details (Section A), other model details (Section B), other implementation details (Section C), additional ablation study (Section D), additional qualitative results (Section E), and limitations of proposed method (Section G).

A. Other Inference-Time Saliency Details

Saliency generation during inference. The Image-Text Matching predicts whether a pair of image and class label is positive (matched) or negative (not matched) (Luo et al., 2024). This is equivalent to asking: *which attention embeddings contribute the most to decide if the image-text pair is matching?* We use a MLP to regress $\hat{y}_{(v,t)}^{itm}$ in Eq. 1 based on the attention maps A as the joint representation of the image-text pair, predicting a two-class probability (matched or not matched). The ITM loss and segmentation supervision are used only during training, while inference relies solely on image-text alignment. At inference, our model uses the gradients of the predicted matching scores, not gradients of the loss. Specifically, we treat the matching score as a scalar objective and back-propagate from it following the standard practice in gradient-based attribution methods (Selvaraju et al., 2017). Note that DiSa doesn't need ground truth segmentation mask, class label, or pixel-level supervision during inference.

Generalization to novel classes. Although the ITM loss is supervised using base classes' masks, it does not learn class-specific saliency patterns. Instead, it trains the model to identify class-agnostic foregroundness, i.e., visually salient structures (edges, textures, object boundaries) that are shared across categories. This supervision regularizes the saliency mechanism to highlight object-centric regions rather than memorizing base classes, which allows it to generalize naturally to novel open-vocabulary classes when combined with class-level correlation maps at inference.

B. Other Model Details

B.1. Upsampling Decoder

We adopt a lightweight upsampling decoder following the design in (Cho et al., 2024). Specifically, we extract intermediate visual embeddings from the 4-th and 8-th layers (Dosovitskiy et al., 2020) of the CLIP ViT-L/14 image encoder (or the 8-th and 16-th layers of CLIP ViT-L/14) for higher-resolution guidance. The decoder consists of two identical transposed convolution layers that progressively upsample the feature maps. It takes the correlation maps with a resolution of 24×24 as input, and outputs predictions at a resolution of 96×96 . The effectiveness of this simple decoder stems from our saliency-aware disentanglement and hierarchical refinement, which models rich contexts while preserving accurate object boundaries, thereby enhancing feature extraction qualities.

Ablation study details. For class-level disentanglement ((II) in Table 3), we use ChatGPT 4o (Achiam et al., 2023) to partition all classes into foreground and background classes with two complementary branches. Similar to our DiSa's design, each branch is processed independently to capture distinct class-specific cues, and the resulting representations are finally merged to form unified embeddings.

C. Other Implementation Details

Training details. We use pre-trained CLIP ViT-B/16 (Radford et al., 2021) as our base-VLM and CLIP ViT-L/14 (Radford et al., 2021) as our large-VLM, following the same setting as in most recent SOTA models (Cho et al., 2024). We train three attention layers for generating saliency maps following the empirical experience and ablation studies in PnP-OVSS (Luo et al., 2024). We adopt settings of 8 heads and dimension size = 512 for these attention layers. For the Pixel-Wise Refinement and subsequent Swin Transformer (Liu et al., 2021) used for aggregation, we adopt a commonly used structure: one non-shifted window attention layer, followed by a shifted window attention layer. Some other training details include Warmup Cosine Learning Rate scheduler (Gotmare et al., 2018) and 1e-4 weight decay.

Data preprocessing. The data augmentation used in our work includes random cropping, and photometric distortion, following (Cheng et al., 2022). During training, saturation, hue, and contrast are randomly adjusted for robustness. The training resolution is set to be 384×384 .

Text template. We utilize the commonly used prompt template for text labels, which is "A photo of a class", without relying on cutting-edge templates. We do not incorporate any LLM-generated or handcrafted prompts in our work.

| k | A-847 | PC-459 | A-150 | PC-59 | PAS-20 | PAS-20 ^b |
|----------|-------------|-------------|-------------|-------------|-------------|---------------------|
| (I) 16 | 11.4 | 18.7 | 32.6 | 57.8 | 96.3 | 78.0 |
| (II) 48 | 12.0 | 19.8 | 34.1 | 58.3 | 97.1 | 78.6 |
| (III) 96 | 12.6 | 20.3 | <u>33.7</u> | 59.3 | 97.0 | 79.9 |

Table 4. Ablation study for foreground selection hyperparameter k .

| | A-847 | PC-459 | A-150 | PC-59 | PAS-20 | PAS-20 ^b |
|--------------------|-------------|-------------|-------------|-------------|-------------|---------------------|
| (I) Attn agg | 12.5 | 20.3 | <u>33.5</u> | 59.0 | 97.3 | 79.4 |
| (II) Hard agg | 12.2 | 19.9 | 32.9 | 58.7 | 96.4 | 80.1 |
| (III) Weighted agg | 12.6 | 20.3 | <u>33.7</u> | 59.3 | 97.0 | 79.9 |

Table 5. Ablation study for foreground/background aggregation designs.

Evaluation metrics. We use mean Intersection over Union (mIoU) to measure segmentation performance. For model efficiency analysis, we use parameter size and GFLOPs.

D. Additional Ablation Study

Design choices of foreground selection k . To further validate the impact of foreground selection hyperparameter, we leverage different k to evaluate our model’s robustness in Table 4: (I) $k=16$ (3% ratio of all tokens), (II) $k=48$ (8% ratio of all tokens), (III) $k=96$ (17% ratio of all tokens). Overall, generally speaking, the performance gradually improves with increasing k , and it yields small but consistent gains when $k=96$, achieving a good balance between expressiveness (for small k) and noise (for large k). PC-459 and A-847 improve the most across k , suggesting they benefit significantly from foreground-background disentanglement. Results on PAS-20 are relatively robust, which reveals that our disentanglement design captures complex scenario understanding and mitigates **Foreground Bias**.

Design choices of foreground/background feature aggregation. We conduct additional experiments that compare (I) Attention-based aggregation, using learnable weights with attention mechanism; (II) Hard aggregation, directly aggregating foreground and background tokens (reorganization with mask indices), and (III) our weighted aggregation (by using learnable weights by gating mechanism). in Table 5. Our design achieves significant improvements, demonstrating our design’s robustness.

E. Additional Qualitative Results

To further validate our model, we present more visualizations of qualitative results on A-150 (Zhou et al., 2019) in Fig. 7, A-847 (Zhou et al., 2019) in Fig. 8, PC-59 (Everingham et al., 2010) in Fig. 9, and PC-459 (Everingham et al., 2010) in Fig. 10. DiSa consistently produces accurate and robust predictions in complex scenarios, demonstrating its efficacy.

We additionally present the comparison of qualitative results on PAS-20^b (Ghiasi et al., 2022) between DiSa and one previous SOTA approach, CAT-Seg (Cho et al., 2024), in Fig. 11. Note that PAS-20^b has one extra “background” class, and the results clearly illustrate our identified limitations and motivations. Specifically, CAT-Seg struggles to (i) separate foreground and background areas (e.g., window in row 1, potted plant in row 2, and sofa in row 5), and (ii) define accurate boundaries between objects (e.g., TV monitor in row 3 and bicycle in row 4). These two limitations correspond to the **Foreground Bias** and **Limited Spatial Localization** inherent in VLMs, respectively. In contrast, DiSa improves foreground-background contexts and generates more precise object boundaries, demonstrating DiSa’s ability to tackle challenging scenarios and mitigate the aforementioned limitations.

F. Failure Cases

We additionally provide a failure case of imperfect foreground/background separation in Fig. 6. In this crowded scene, some salient regions of the class “person” are not assigned as the foreground. It demonstrates that, for objects that vary widely in size, the disentanglement might become unstable, leading to inaccurate or ambiguous foreground/background separation. However, the ensemble nature of our dual branches provides robustness by preserving complementary cues in the alternative branch compensate for such errors, leading to more reliable fused predictions.

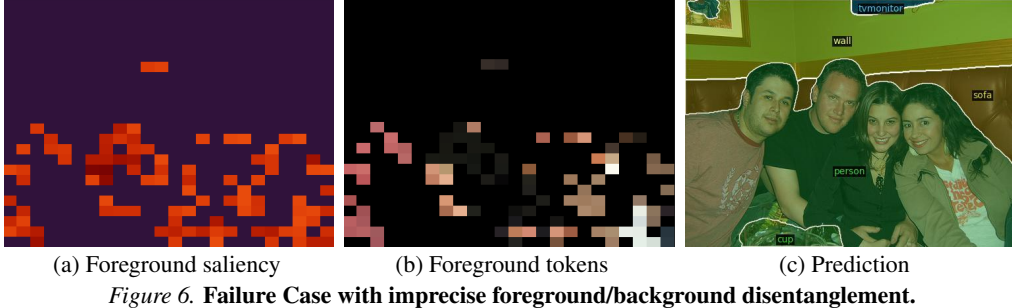


Figure 6. Failure Case with imprecise foreground/background disentanglement.

G. Limitation

Our foreground selection hyperparameter k is fixed and we plan to make it adaptive. Instead of selecting a constant number of foreground tokens for all images, we will predict a dynamic k conditioned on the input image, e.g., using saliency/uncertainty statistics or a lightweight gating module, to reflect varying object scales and scene complexity. This input-dependent token allocation can better balance foreground–background evidence, reduce sensitivity to hyperparameters, and further improve robustness across diverse open-vocabulary scenes.

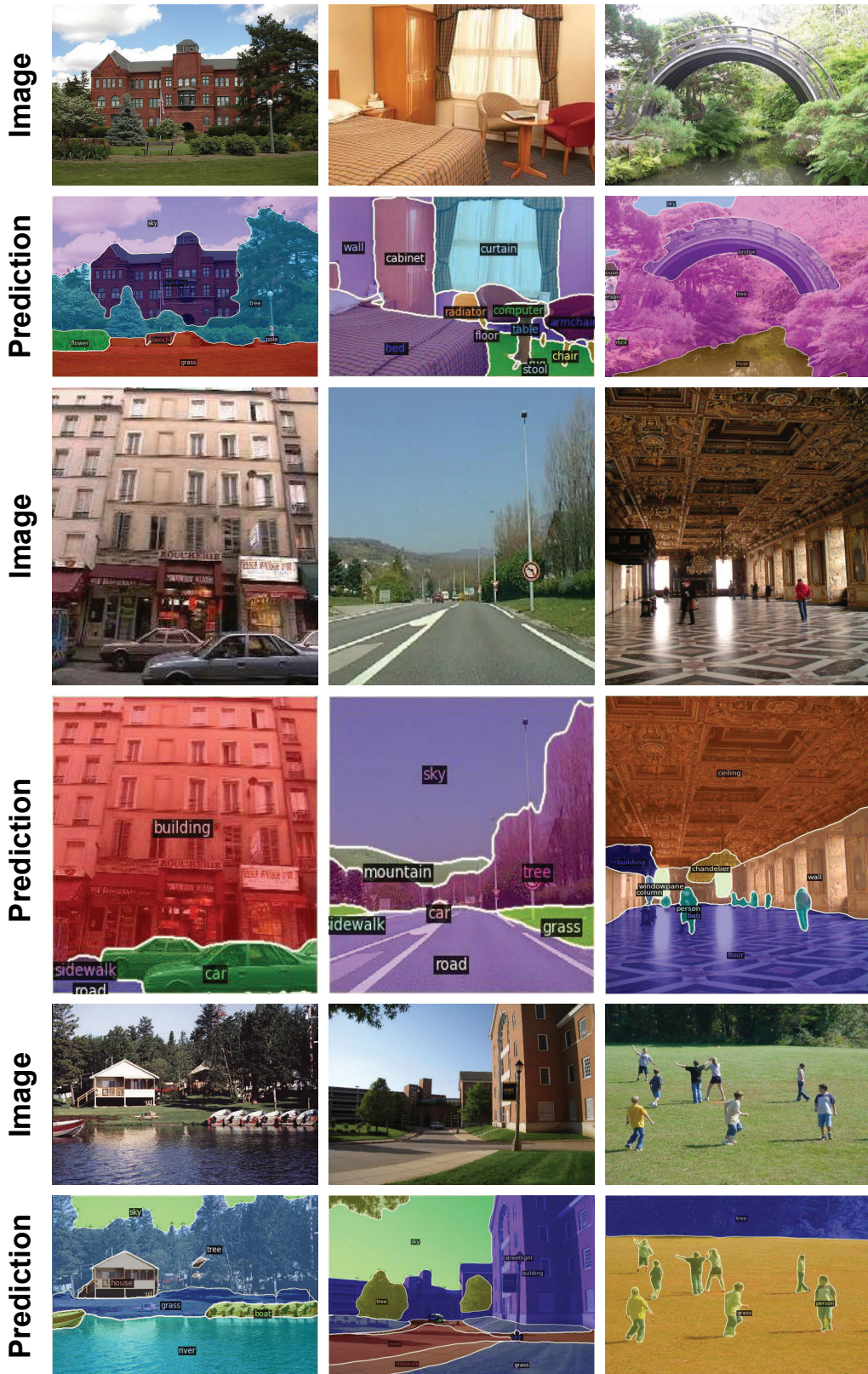


Figure 7. Qualitative results on ADE20K with 150 classes.

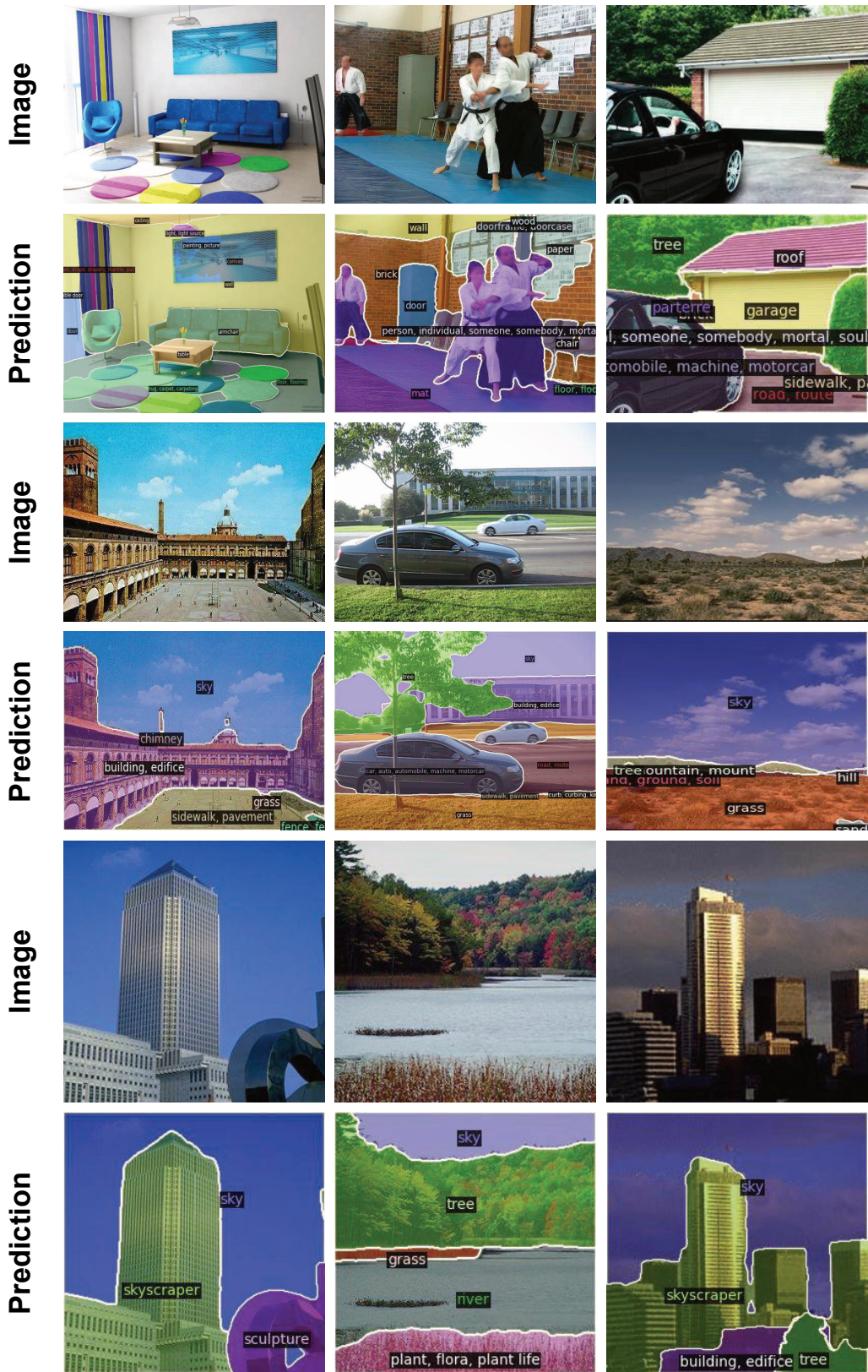


Figure 8. Qualitative results on ADE20K with 847 classes.



Figure 9. Qualitative results on PASCAL Context with 59 classes.

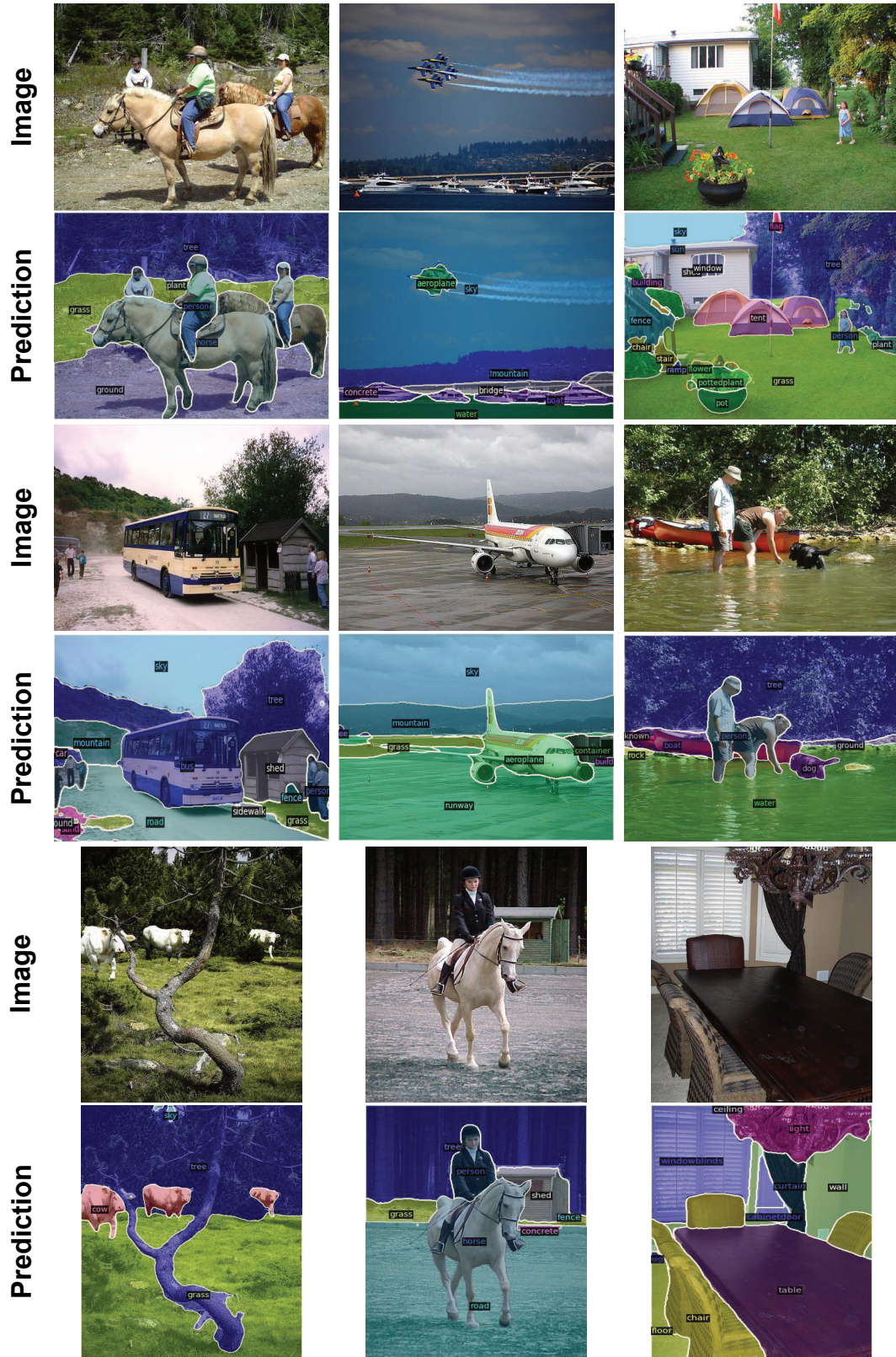


Figure 10. Qualitative results on PASCAL Context with 459 classes.

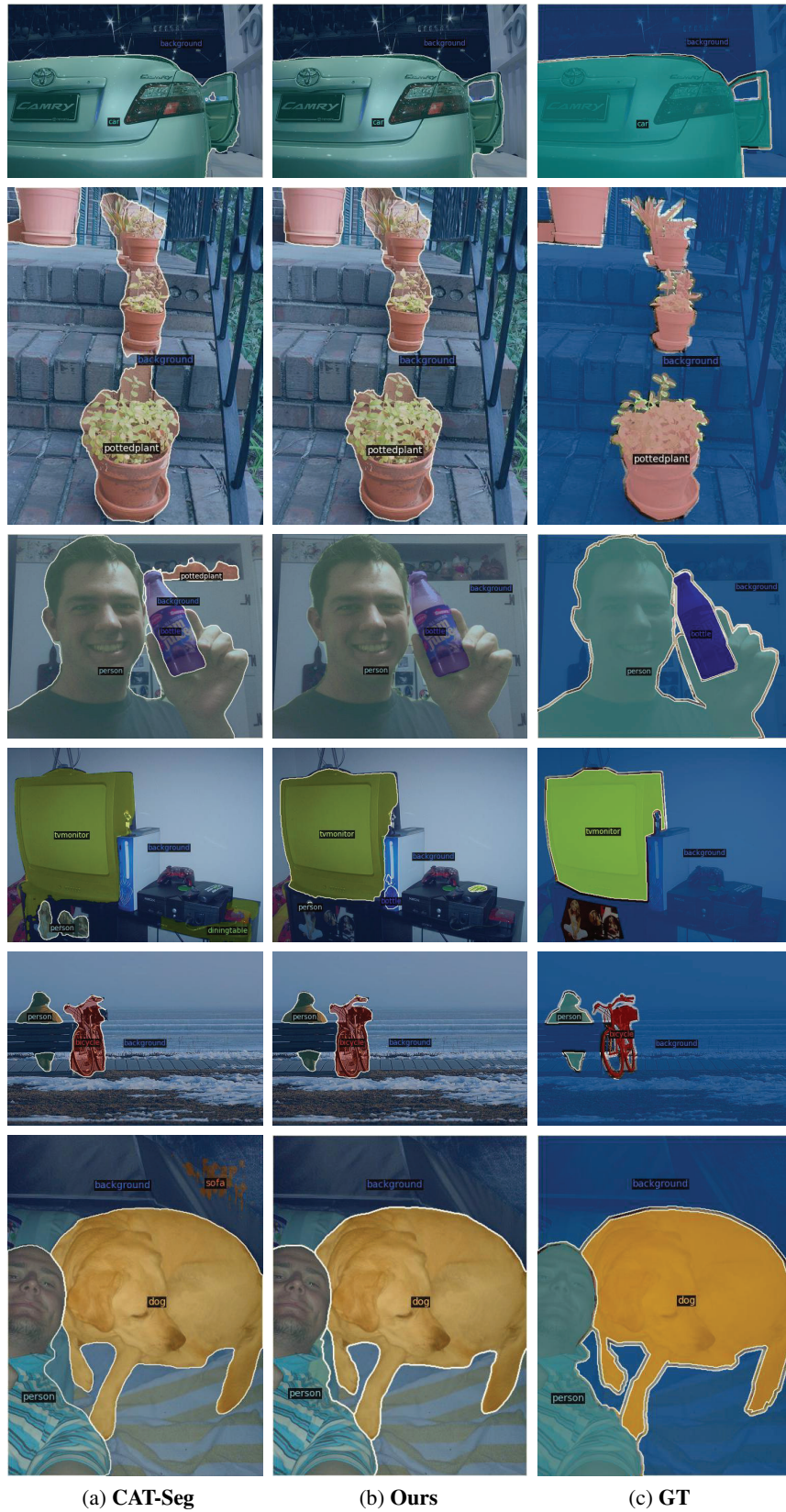


Figure 11. Comparison of Qualitative results on PAS-20^b. We compare DiSa with CAT-Seg.